No longer is general relativity " a theorist's Paradise, but an experimentalists Hell"

It is now a Paradise for all .....

C. Misner, K. S. Thorne and J.A Wheeler   *"Gravitation"* P 1131 (1973)

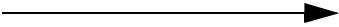# Some adventures in experimentalist's heaven
at Kip's Fest, June 1, 2000
Rainer Weiss

OUTLINE

1)   Experimental relativity

2)   Case study in observational relativity - deflection of light

3)   Case study in experimental relativity - the weak principle of equivalence

4)   Gravitational radiation - a combination of experiment and observation

5)   Kip's flirtations with being an experimenter

THE PARADISE OF EXPERIMENTAL RELATIVITY

OBSERVATION $\longrightarrow$ EXPERIMENT

Fundamental Tests

Variation of "constants" with epoch

Variation of constants with grav. potential
Weak principle of equivalence
New long range couplings

Gravitation obeys weak principle?

Weak Field Phenomena

Comparison of clocks at different gravitational potential
Deflection of light
Retardation of light in the gravitational potential
Dynamics of massive bodies

Magnetic gravitation/frame dragging
Periodic gravitational waves

Radar ranging

Intermediate Field Phenomena

Compact binary systems

Strong Field Phenomena

X ray binary emission
Formation of black holes
Primeval density fluctuations
Universe as a single system

Impulsive and stochastic gravitational waves

Kip: Allowing General Relativity to be testable and not remain a monolith.
Bringing Caltech into Experimental Relativity

THE CHALLENGE FOR THE EXPERIMENTER AND OBSERVER

Real challenges

- Understanding and elimination of the extraneous noise sources.
- Measurement at the fundamental limits of the technique.
- Control of and test for systematic errors.
- Making the time to "do it right".

Social challenges

- The strong expectation that the theory is correct.
- The subconscious impetus to iterate to the "correct" result.
- Being less critical when the result is "correct".

THE SALVATION FOR THE EXPERIMENTER AND OBSERVER

- A discovery in astrophysics of a new class of systems and phenomena.
- Advances in technology.
- A discovery of a new phenomena with high relative precision.
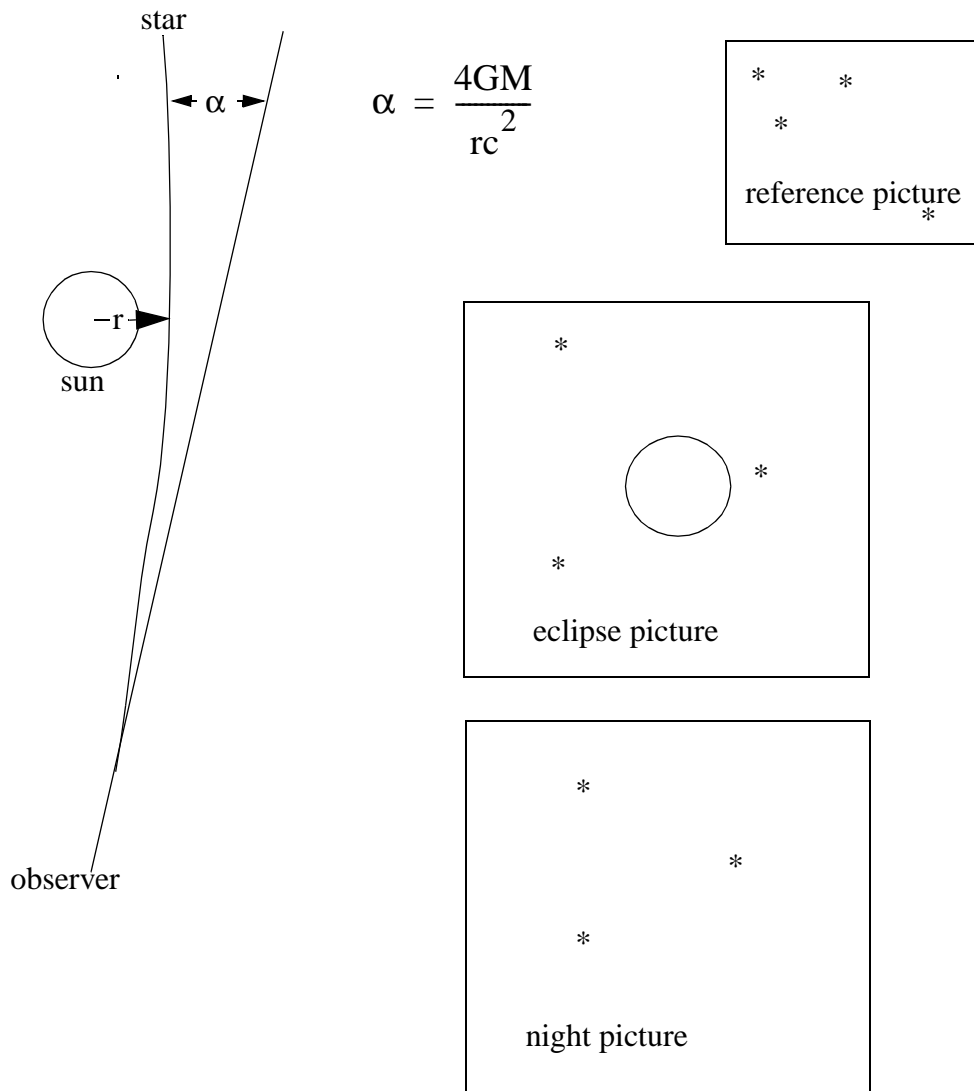- Getting the time to "do it right".
- Sometimes a good idea.

CASE STUDY 1: THE DEFLECTION OF LIGHT

References:

"The Determination of Einstein's Light-Deflection in the Gravitational Field of the Sun"
H. von Klüber in *VISTAS IN ASTRONOMY* V3, 47 (1960)

"A Confirmation of Einstein's General Theory of Relativity by Measuring the Bending of Microwave Radiation in the Gravitational Field of the Sun" E.B. Fomalont and R.A. Sramek , *Astrophysical Journal* V199,749 (1975)

"Further Experimental Tests of Relativistic Gravity Using the Binary Pulsar PSR 1913 + 16"
J.H. Taylor and J. M. Weisberg, *Astrophysical Journal* V345, 434 (1989)

$$\alpha = \frac{4GM}{rc^2}$$

star

α

−r−

sun

observer

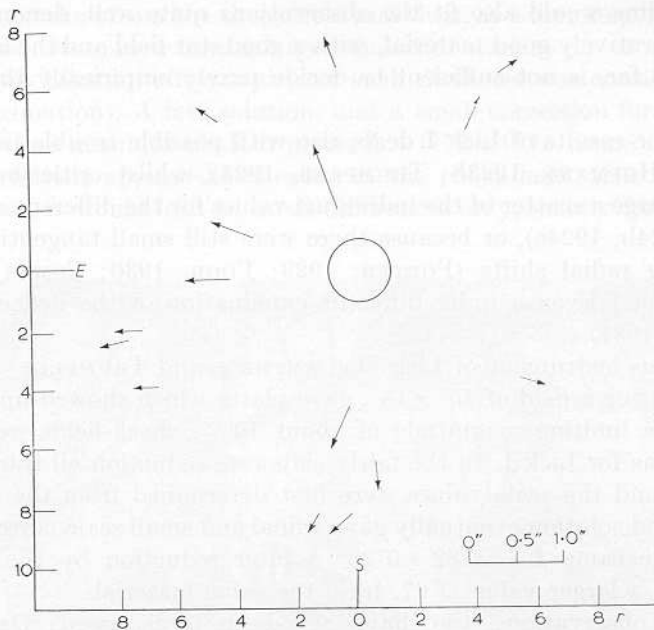reference picture

eclipse picture

night picture

FIG. 9. Vector diagram of the radial shifts, derived from means of the 15 best stars by the Lick I and Lick II observations in 1922. It presents a very good indication of the existence of the light-deflection (CAMPBELL and TRUMPLER, 1928)
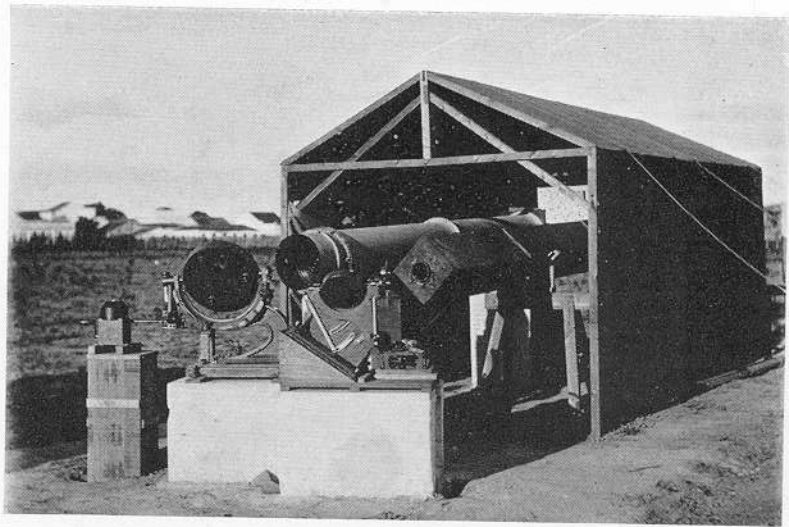
FIG. 7. The instrument used by the Greenwich expedition in 1919 at Sobral (Brazil). The two coelostats are feeding two horizontal telescopes: $f = 343$ cm and aperture 20 cm, on the left; $f = 570$ cm and 10 cm aperture, on the right; DYSON, EDDINGTON and DAVIDSON, 1920. (Photo. C. R. DAVIDSON.)
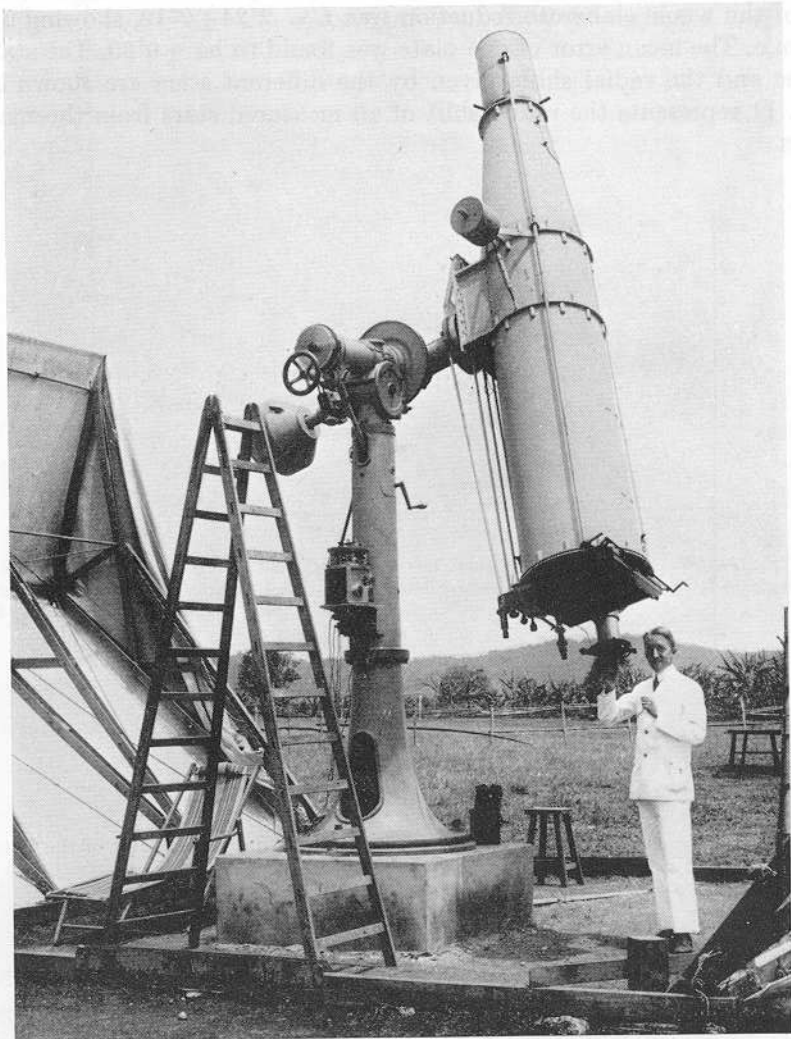
Fig. 12. Large parallactically mounted Zeiss astrograph ($f = 343$ cm, 20 cm aperture) with electrically controlled automatic drive, covering the large field of $7°.5 \times 7°.5$, as used in 1929 by the Potsdam observers (Potsdam II). During the eclipse itself a check star-field was photographed on each of the three plates taken of the Sun's surrounding, by pointing the astrograph alternately at a star-field distant from the Sun (FREUNDLICH, v. KLÜBER, v. BRUNN, 1933). (Photo: v. KLÜBER.)
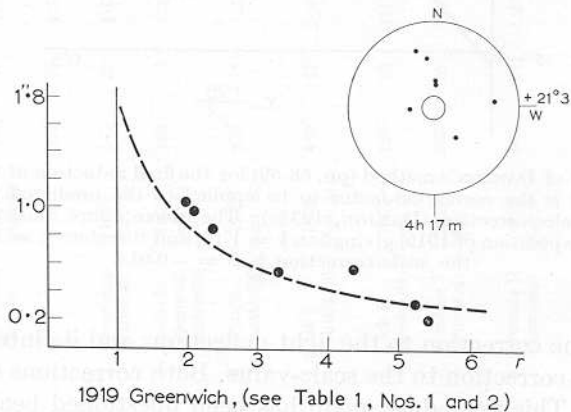
Table 1

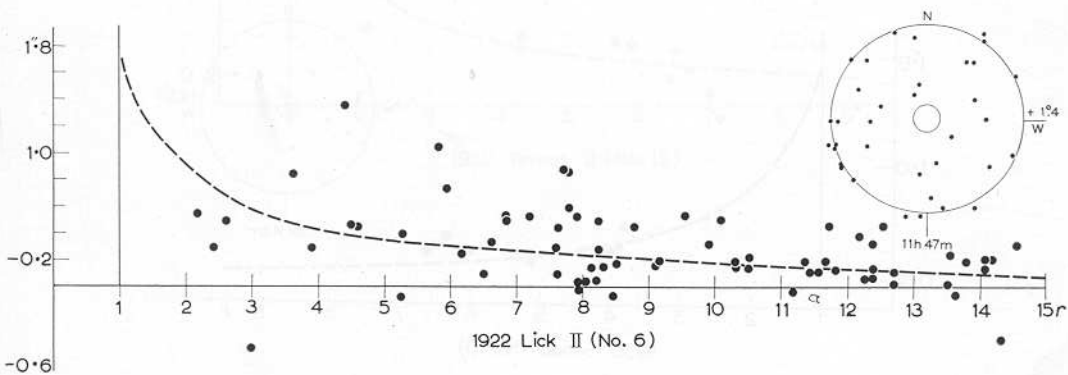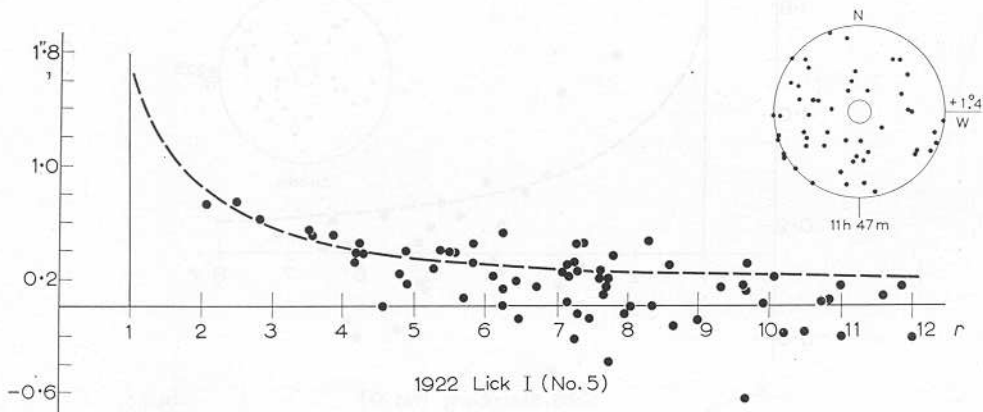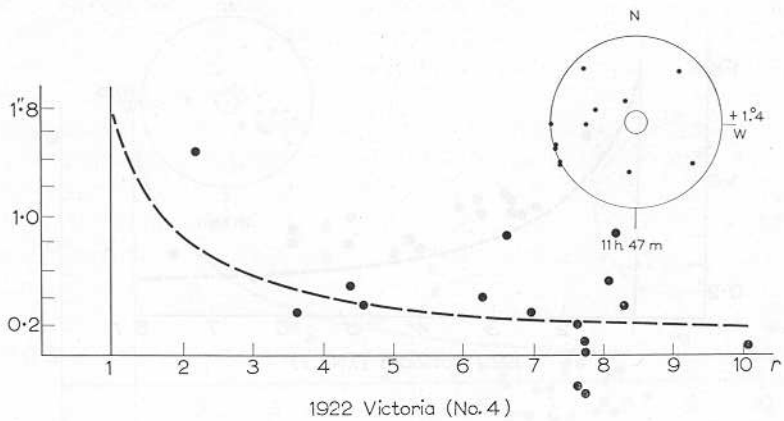| 1	2 Observatory (site)	3 Eclipse	4 Focal length f (cm)	5 Aperture ϕ (cm)	6 ϕ/f	7 Instrument (lens)	8 Field of plate	9 Number of plates	10 Exposure (sec)	11 Limiting stellar magnitude	12 Number of stars	13 r_{min} (solar radii from centre)	14 r_{max} (solar radii from centre)	15 Check-field	16 L	17 m.s.e.	18 Reference
1	Greenwich (Brazil)	1919 May 29	570	10	1:57	Coelostat (Double)	2°4x2°0	7	28	6(ph)	7	2	6	no	1″.98	0″.16	DYSON-EDDINGTON-DAVIDSON, 1920
			343	20	1:17	Coelostat (Double)	2·7×2·7	16	5–10	6(ph)	11	2	6	no	0·93	—	
2	Greenwich (Principe)	1919 May 29	343	20	1:17	Coelostat (Double)	2·7×2·7	2	2–20	6(ph)	5	2	6	no	1·61	0·40	
3	Adelaide-Greenwich (Australia)	1922 Sept. 21	160	7·5	1:21	Astrograph (Quadruple)	7×8	2	20–30	8·3	11–14	2	10	yes	1·77	0·40	DODWELL-DAVIDSON, 1924
4	Victoria (Australia)	1922 Sept. 21	330	15	1:22	Astrograph (Quadruple)	—	2	45	9·0	18	2	10	not used	1·75 1·42 2·16	—	CHANT-YOUNG, 1924.
5	Lick I (Australia)	1922 Sept. 21	450	12	1:37	Doubl. Astrograph (Double)	5×5	4	120–125	10·5(ph)	62–85	2·1	14·5	yes	1·72	0·15	CAMPBELL-TRUMPLER, 1923a.
6	Lick II (Australia)	1922 Sept. 21	150	10	1:15	Astrograph (Quadruple)	15×15	6	60–102	10·4(ph)	145	2·1	42	yes	1·82	0·20	CAMPBELL-TRUMPLER, 1928
7	Potsdam I (Sumatra)	1929 May 9	850	20	1:42	Coelostat (Double)	3×3	4	40–90	8·9	17–18	1·5	7·5	yes	2·24	0·10	FREUNDLICH-v. KLÜBER-v. BRUNN, 1931a.
8	Potsdam II (Sumatra)	1929 May 9	343	20	1:17	Astrograph (Triplet)	7·5×7·5	3	14–56	9·5	84–135	4	15	yes	—	—	FREUNDLICH-v. KLÜBER-v. BRUNN, 1933.
9	Sternberg (U.S.S.R.)	1936 June 19	600	15	1:40	Astrograph (Double)	3·5×3·5	2	25–35	9·6	16–29	2	7·2	not used	2·73	0·31	MIKHAILOV, 1949.
10	Sendai (Japan)	1936 June 19	500	20	1:25	Coelostat (Double)	2·9×2·9	2	80	8·6 (vis.)	8	4	7	no	2·13 1·28	1·15 2·67	MATUKUMA, 1940a.
11	Yerkes I (Brazil)	1947 May 20	609	15	1:40	Astrograph (Triplet)	4×4	1	185	10·2	51	3·3	10·2	not used	2·01	0·27	VAN BIESBROECK, 1949.
12	Yerkes II (Sudan)	1952 Feb. 25	609	15	1:40	Astrograph (Triplet)	4×4	2	60–90	8·6	9–11	2·1	8·6	yes	1·70	0·10	VAN BIESBROECK, 1953

Fig. 6. These 9 combined diagrams show the actually measured light-deflections for each star, as far as available, using only the data given by the authors themselves, without having regard to individual weights or group-means. Some small amendments, mainly due to scale correction, may have to be applied to the one or the other of these observational sets. The broken hyperbola represents the Einstein Effect as it should be expected from theory.
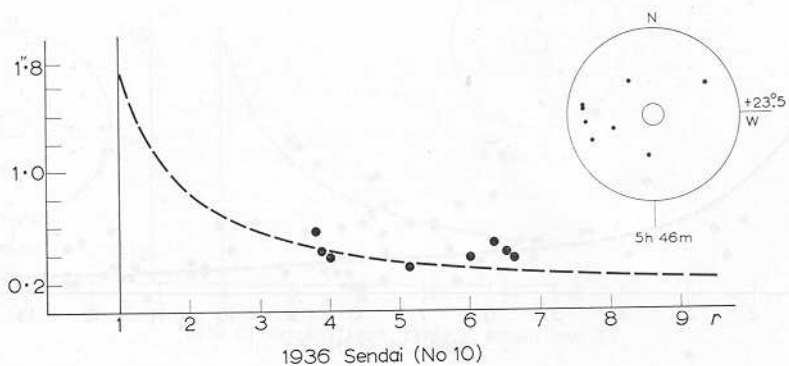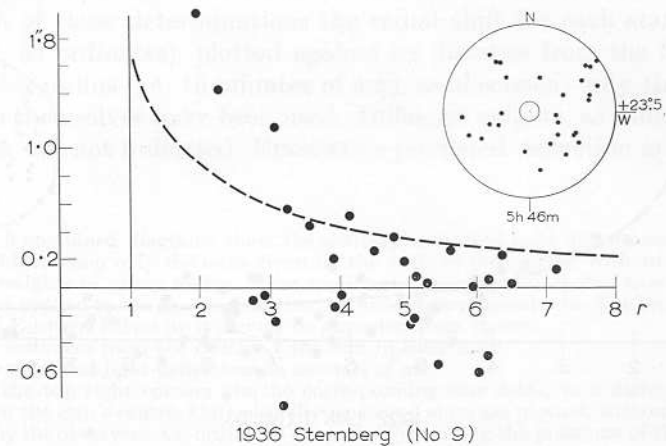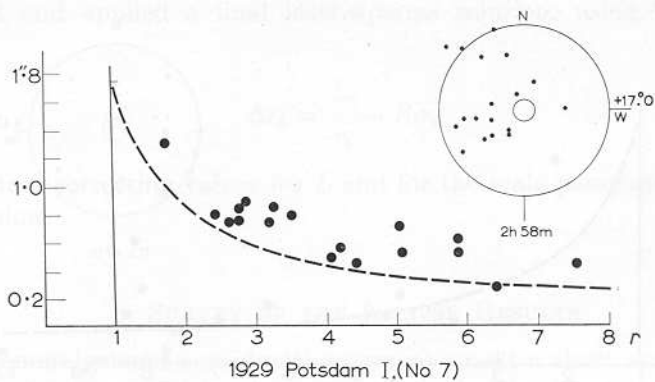
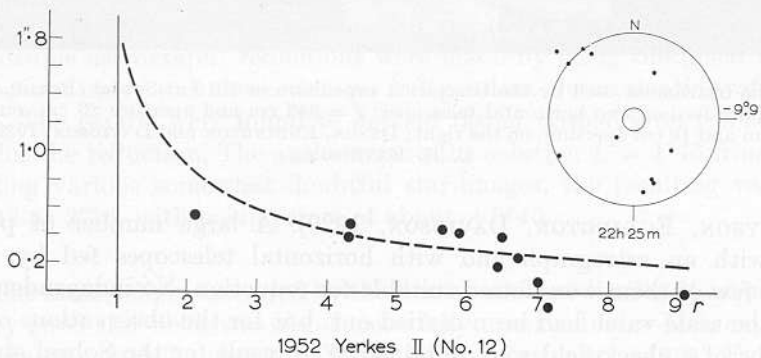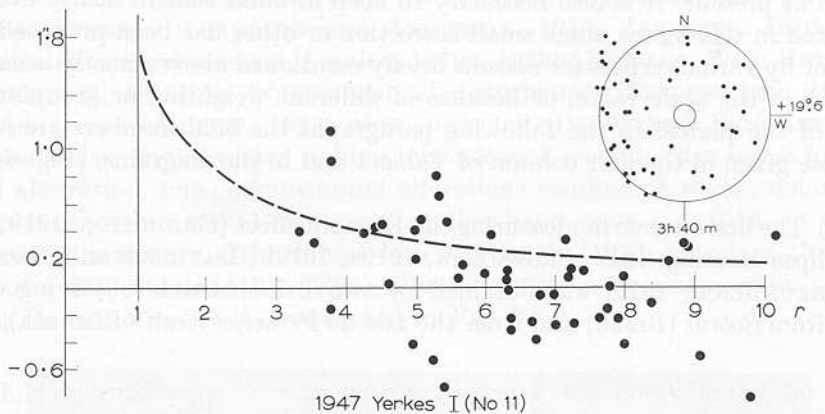*Abscissae*: distances from the centre of the Sun in solar radii.

Ordinates: measured light-deflections in seconds of arc.

Inserted into the top right corners are the corresponding star fields, to a distance of about 8 solar radii from the Sun's centre. Only actually measured stars are plotted, without regard to the weight given by the observers. Co-ordinates are indicated, giving the positions of the Sun's centre for 1855·0 (B.D.-charts).

1919 Greenwich, (see Table 1, Nos. 1 and 2)

1922 Victoria (No. 4)

1922 Lick I (No. 5)

1922 Lick II (No. 6)

1929 Potsdam I.(No 7)

1936 Sternberg (No 9)

1936 Sendai (No 10)

1947 Yerkes I (No 11)

1952 Yerkes II (No. 12)

Fitting procedure for difference between stellar positions in the plates
    relative translation
    relative rotation
    inclination of each plate relative to the telescope optic axis
    scale value (magnification)
    light deflection

Most significant difficulty - maintaining the scale

$$30\% \quad \text{measurement} \quad @ \quad r = 5 \quad \longrightarrow \quad \Delta\alpha = 0.1\,\text{sec}$$

$$\frac{\Delta f}{f} = \frac{\Delta L}{L} \leq 4 \times 10^{-6}$$

    Inevitable thermal instabilities during the eclipse

Other difficulties

Not enough bright stars within the significant fitting region to separate scale from deflection.
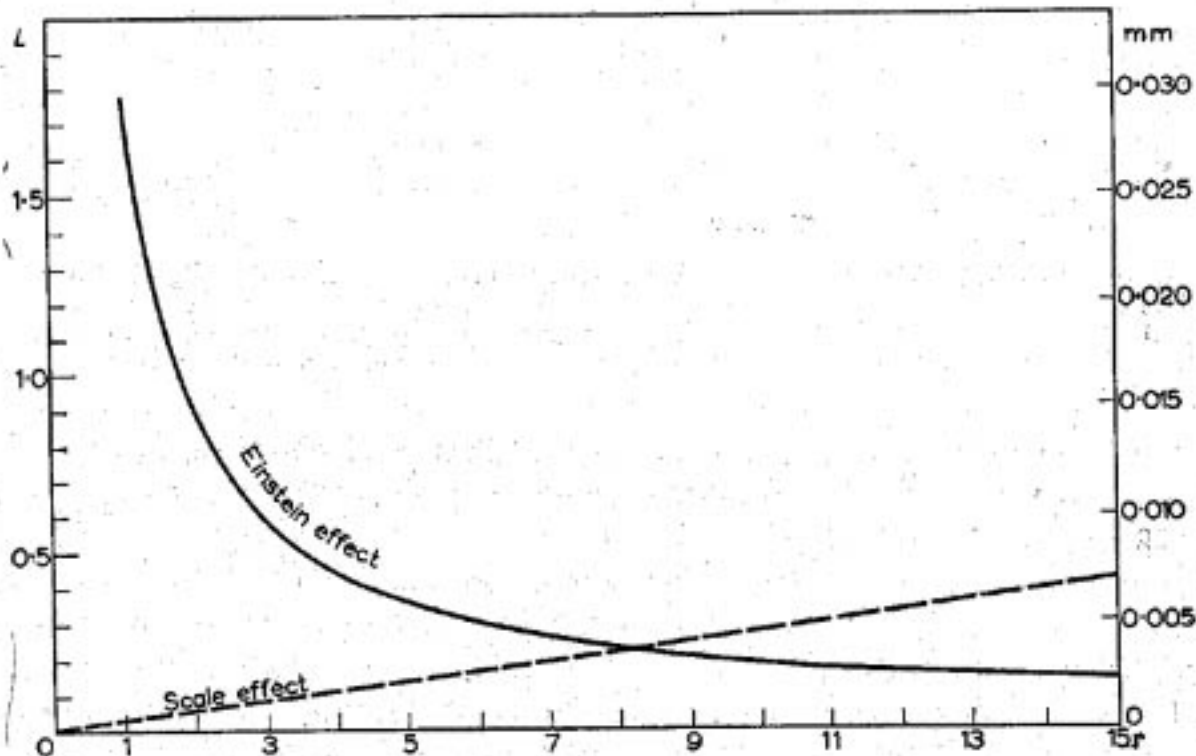Not enough observing time: 90 minutes total 1919 - 1960

Fɪɢ. 2. This graph, a hyperbola, shows the behaviour of the predicted light-deflection, plotted as a function of the distance r from the centre of the Sun. The broken straight line indicates the "Scale Effect" (see p. 53), produced by an alteration of 0·1 mm in the focal setting of a "Normal Astrograph" ($f = 343$ cm).

Abscissae: distances from the centre of the Sun, expressed in units of the solar radius.
Left-hand ordinate: light-deflections in seconds of arc, as predicted by Eɪɴꜱᴛᴇɪɴ (1916). See eq. (2).
Right-hand ordinate: the same, but expressed in millimetres on the photophraphic plate, assuming the focal length of the telescope to be 343 cm.
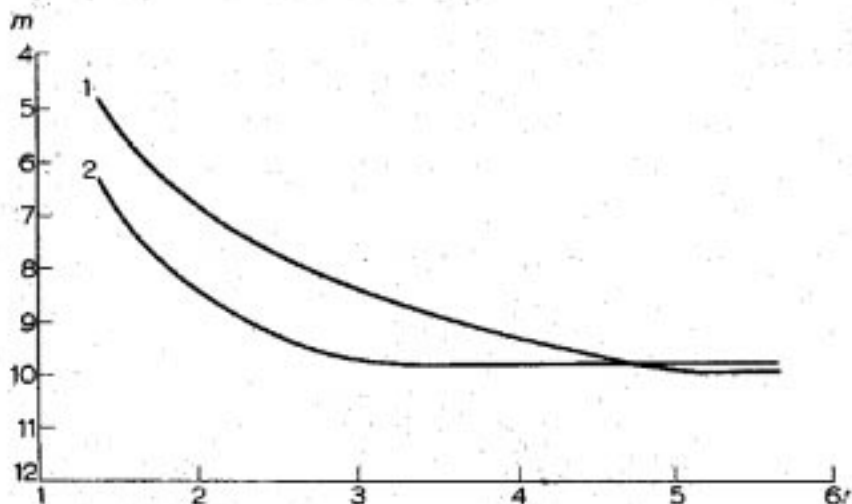
Fig. 3. This diagram indicates in a general manner the faintest stellar magnitude m which may on the average, be recorded on an eclipse photograph, taken with 60 seconds exposure time under favourable conditions, plotted as a function of the distance r of the star from the Sun's centre. (1) Telescope of 20 cm aperture and focal length $f = 343$ cm; (2) telescope of 20 cm aperture and $= 850$ cm. *Abscissae*: distances from the centre of the Sun in solar radaii. *Ordinates*: faintest stellar magnitude to be expected. (v. KLÜBER, 1932b).

BENDING BY MICROWAVE INTERFEROMETRY

$\lambda = 3.7, 11.1$ cm
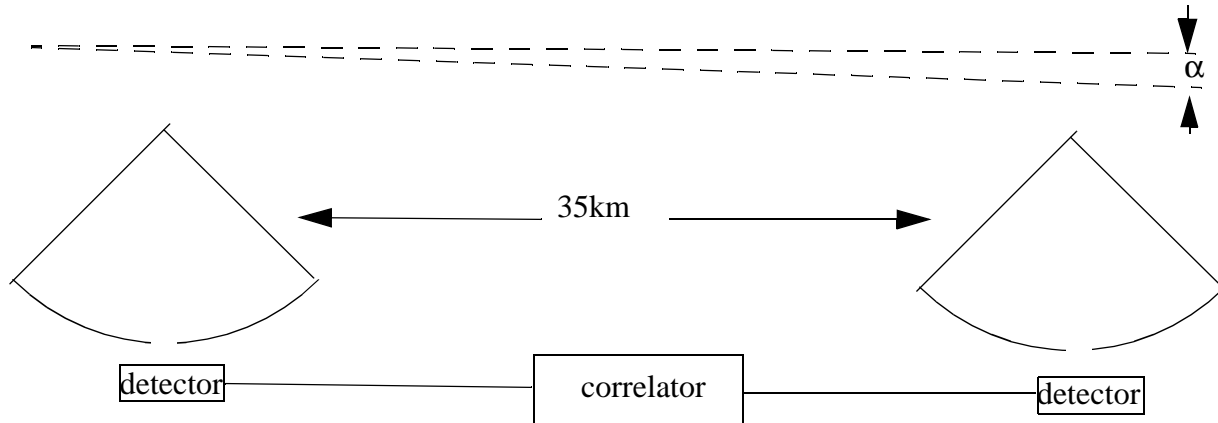
Sensitivity:

$$\Delta\alpha \approx \frac{\lambda}{L} = 1\times10^{-5} = 2 \text{ seconds of arc}$$

Split fringe to 0.004 arc seconds in 8 hours of observation

Perturbations

Solar plasma: refraction varies as $\frac{1}{\omega^2}$. Separate by using two different wavelengths

Atmospheric propagation

Control

Measure relative motion of 0116+08, 0119+11 and 0111+02
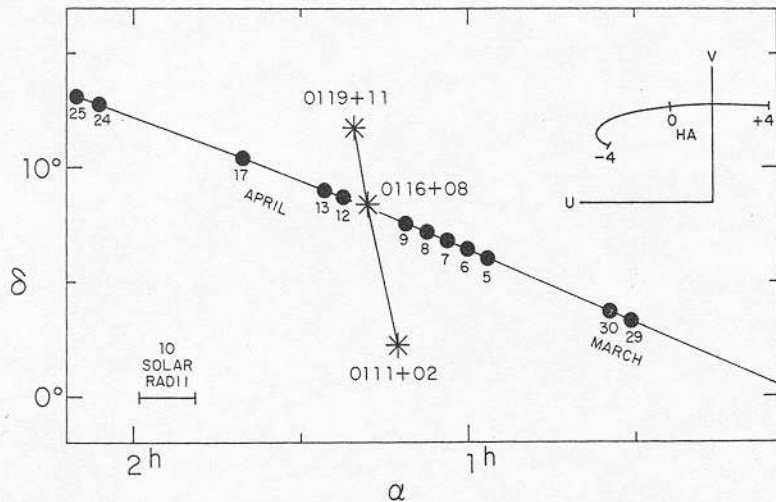
FOMALONT AND SRAMEK

Fig. 1.—The 1974 experiment. The position of the three radio sources and the position of the Sun at noon on each observing day are shown. The coordinates refer to the epoch of date. The projected resolution of the interferometer with hour angle (HA) is given by the (u-v) plot in the upper right.
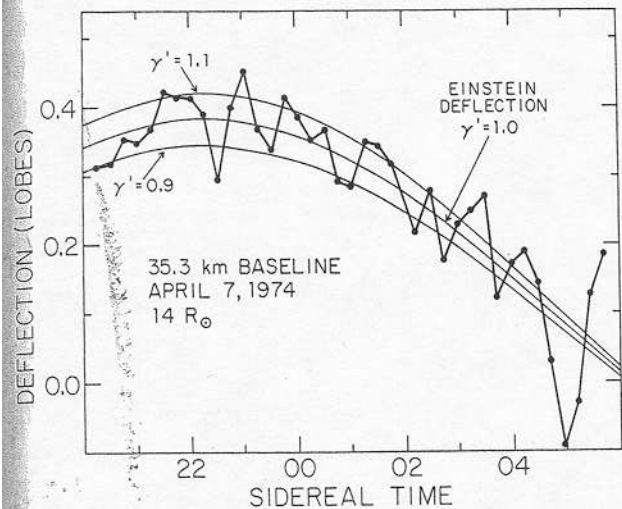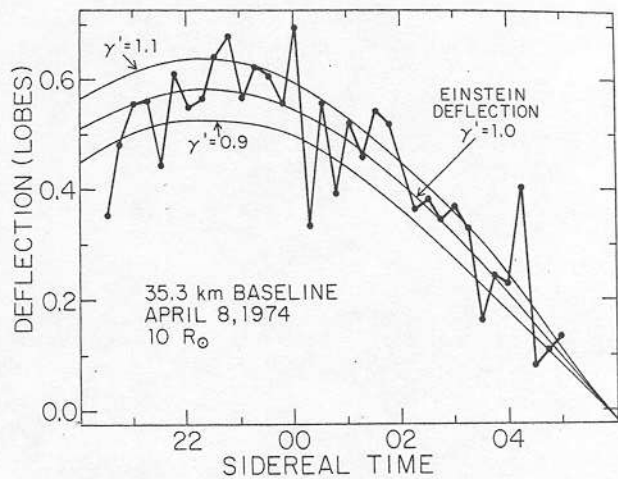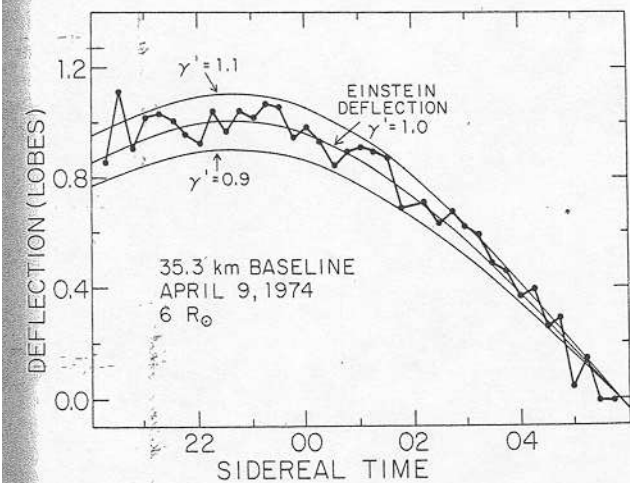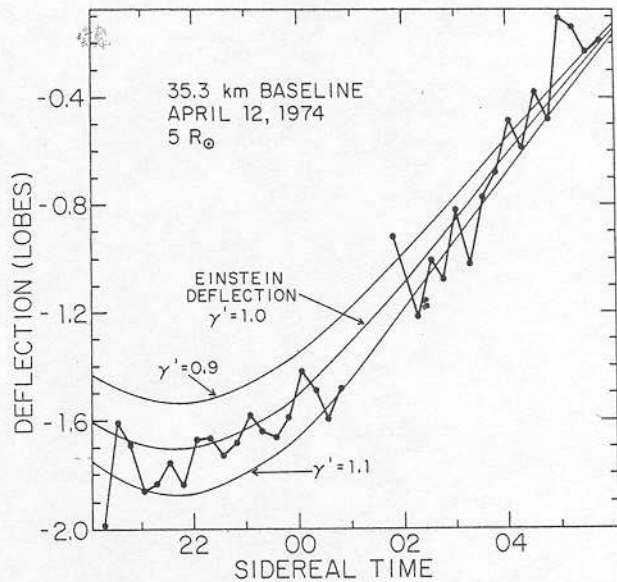
FIG. 3.—The measured corrected phase compared with the phase expected for various deflections for (a) April 7, (b) April 8, (c) April 9, and (d) April 12. All plots are for the 35.3 km baseline, left-hand polarization. The approximate distance of 0116+08 from the Sun is also given. The average phase for each determination every 15 minutes is shown by the dots.
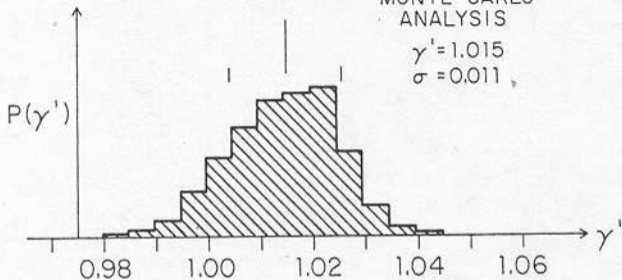
FIG. 4.—The distribution of γ', the coefficient of bending, based on a Monte Carlo analysis of the residual data. The skewness in the distribution is real and reflects the skewness of the distribution of γ' in Table 2. Only the range, not the value, of γ' was determined by this analysis.

BENDING FROM THE BINARY PULSAR

orbit 7.75 hr period

PULSAR 59 ms period

$e = 0.617$

169 pc/cm^3

Arecibo Observatory
@ 430 Mhz, 1410 Mhz

TAYLOR AND WEISBERG
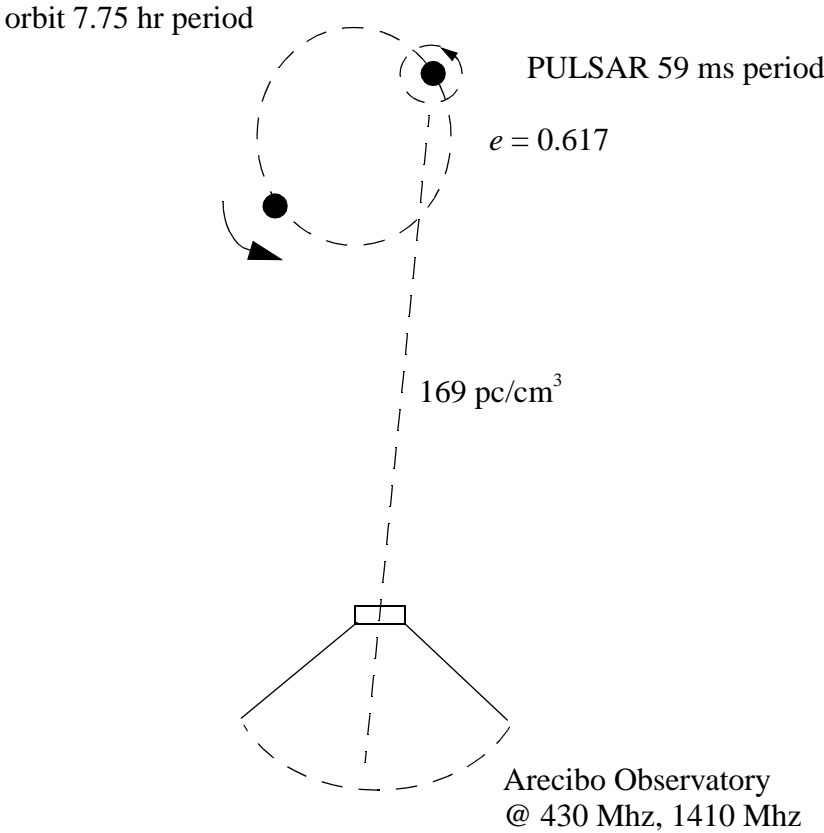
FIG. 1.—Average pulse profiles obtained for PSR 1913+16 over the period 1974–1981, at 430 MHz and 1410 MHz. The changes in shape are the result of improved dispersion removal techniques and consequent improvements in time resolution, as indicated by the horizontal bars.

TABLE 1

OBSERVING SYSTEMS USED AND SUMMARY OF AVAILABLE DATA

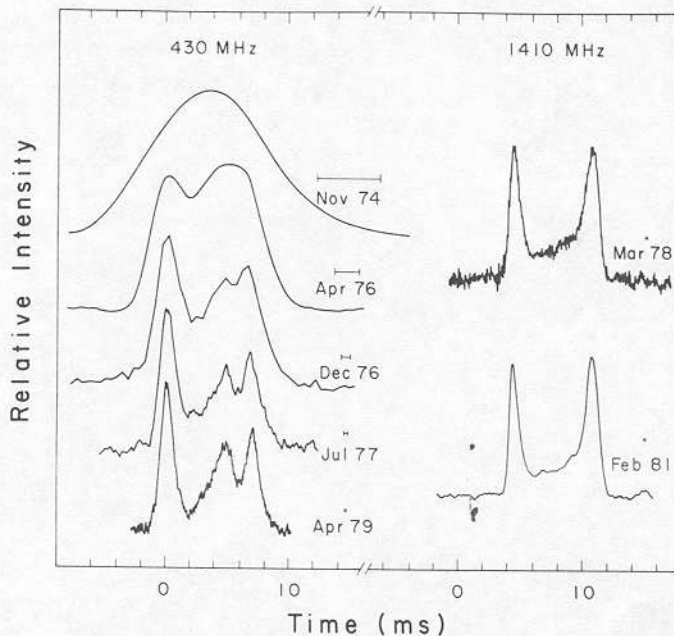| Dates	Frequency (MHz)	Total Bandwidth (MHz)	Frequency Channels	System Noise Temperature (K)	Time Resolution (μs)	TOA Uncertainty (μs)	Number of Observations
A. 1974 Sep–Dec[a]	430	8.0	32	175	5000	275	524
B. 1975 Apr–1976 Nov[b]	430	0.64, 3.2	32	175	2000	310	112
C. 1975 Jun–1976 Feb	430	0.25	1	175	2000	890	75
D. 1976 Nov–Dec[a,b]	430	0.64	32	175	750	155	73
E. 1977 Jul–Aug[b]	430	0.64	32	175	340	150	52
F. 1978 Jun–1981 Feb	430	3.34	504	175	43	75	573
G. 1977 Jul–Aug	1410	8.0	32	80	125	75	57
H. 1977 Dec	1410	8.0	32	80	125	55	72
I. 1978 Mar–Apr[a]	1410	8.0	32	80	125	50	116
J. 1980 Jul–1981 Feb	1410	8.0	32	80, 40	200	85	312
Mark I. 1981 Feb–1984 Dec	1410	16.0	64	40	125	20	1719
Mark II. 1984 Oct–1988 Jul	1408	8.0	32	40	125	31	638
Mark III. 1988 Jul–	1404	40.0	32	40	640	16	159

[a] Raw data samples were recorded on magnetic tape, with signal averaging done afterward in software. All other observations used real-time signal averaging, synchronized by means of a precomputed ephemeris.

[b] Some or all of these observations were made with only one polarization.

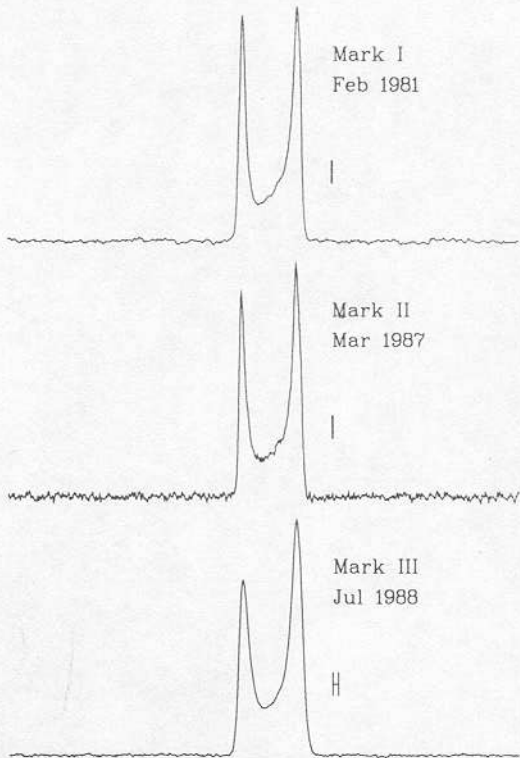Fig. 1.—Average profiles of PSR 1913+16 as observed with the Mark I, Mark II, and Mark III data acquisition systems at frequencies near 1408 MHz. The effective time resolutions, which are dominated by dispersion smearing, are indicated by bars to the right of each pulse. The full period (59.03 ms) is plotted, and the gradual weakening of component 1 relative to component 2 is a real effect (Weisberg, Romani, and Taylor 1989).

TABLE 2

PARAMETERS OF THE TIMING MODELS

Parameter	Single Pulsar	BT Model	EH Model	DD Model	DDGR Model
α	Y	Y	Y	Y	Y
δ	Y	Y	Y	Y	Y
μ_α	Y	Y	Y	Y	Y
μ_δ	Y	Y	Y	Y	Y
t_0	Y	Y	Y	Y	Y
$v = 1/P$	Y	Y	Y	Y	Y
$\dot{v}$	Y	Y	Y	Y	Y
$\ddot{v}$	Y	Y	Y	Y	Y
$x = (a_1 \sin i)/c$	...	Y	Y	Y	Y
e	...	Y	Y	Y	Y
T_0	...	Y	Y	Y	Y
P_b	...	Y	Y	Y	Y
ω_0	...	Y	Y	Y	Y
$\dot{\omega} = 2\pi k/P_b$	...	Y	Y	Y	...
γ	...	Y	Y	Y	...
$\dot{P}_b$	...	Y	Y	Y	...
$s = \sin i$	...	...	Y	Y	...
r	...	...	...	Y	...
$M = m_1 + m_2$	...	...	...	...	Y
m_2	...	...	...	...	Y
$\dot{x}$	...	Y	Y	Y	...
$\dot{e}$	...	Y	Y	Y	...

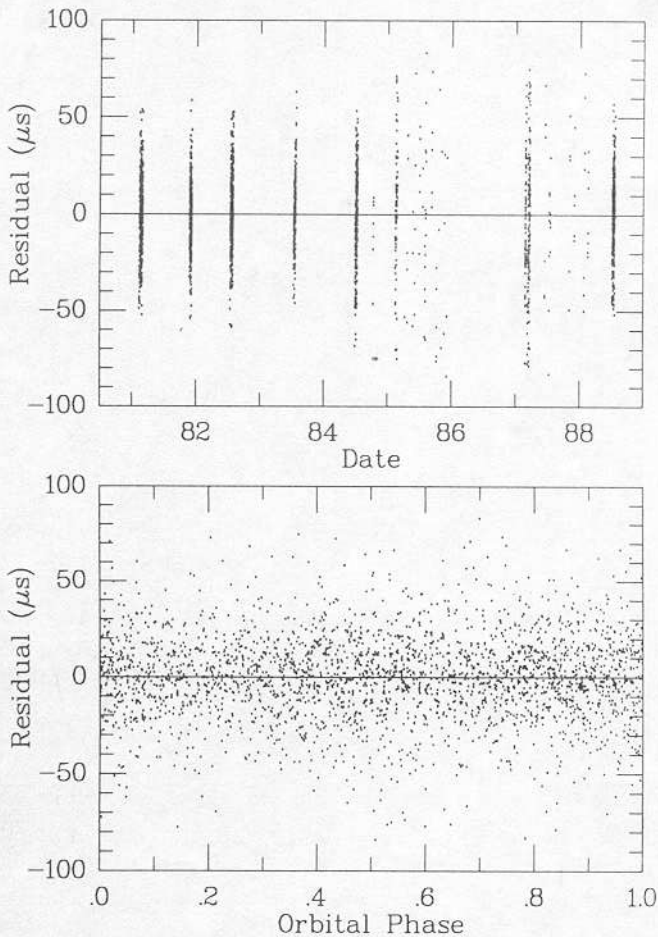NOTE.—"Y" denotes inclusion of the parameter in the model.

FIG. 2.—Postfit residuals from the DD(1) solution in Tables 4 and 5, plotted separately against date and orbital phase.
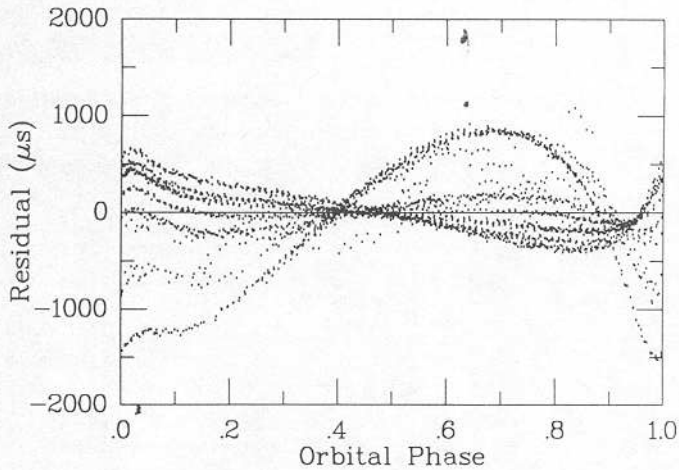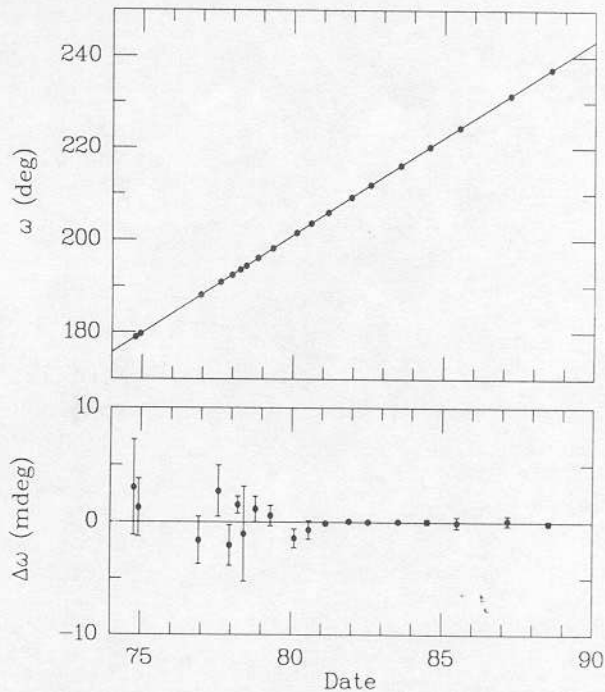
FIG. 3

FIG. 4
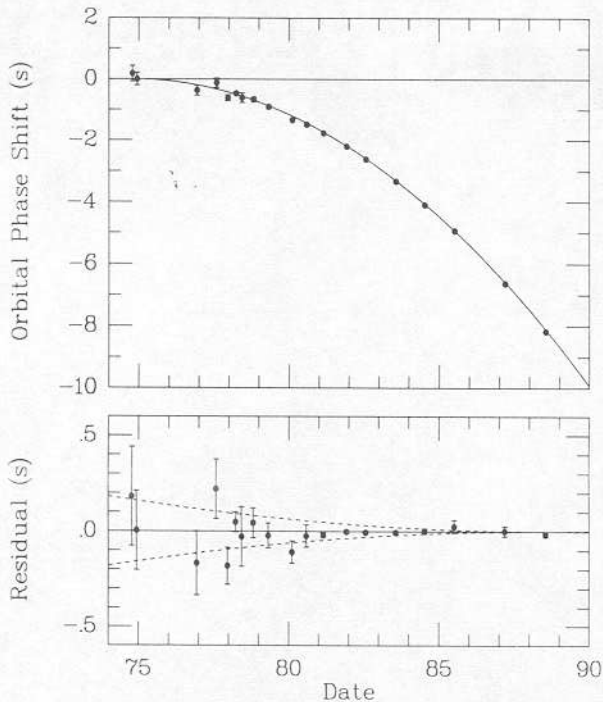
Fig. 5.—*Top*: Cumulative shift of the times of periastron passage relative to a nondissipative model in which the orbital period remains fixed at its 1974.78 value. *Bottom*: Differences between the locally measured periastron times and those expected according to the DD(1) parameter set. Dashed curves illustrate differential trends that would be expected (relative to epoch 1988.54) if the rate of orbital decay $\dot{P}_b$ were 2% larger or 2% smaller.
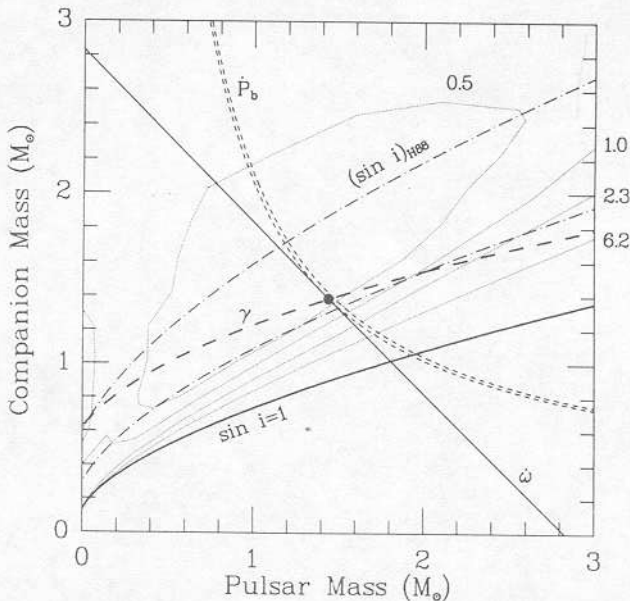
FIG. 9.—Restrictions on the pulsar mass, m_1, and companion mass, m_2, imposed by general relativity are indicated by curves labeled $\dot{\omega}$, γ, $\dot{P}_b$, and $(\sin i)_{H88}$ (the Haugan 1988 sin i parameter). Uncertainties in $\dot{\omega}$ and γ are smaller than the widths of their plotted curves; two curves are plotted for $\dot{P}_b$, and $(\sin i)_{H88}$, bracketing the uncertainty range. Numerically labeled dotted curves represent a mapping of $\Delta\chi^2$ contours for parameters r and s from Fig. 7. Companion masses below the curve labeled sin $i = 1$ are incompatible with the mass function. The point marked with a filled circle corresponds to the mass values given for the DDGR solution in Table 5.

CASE STUDY 2: WEAK PRINCIPLE OF EQUIVALENCE TESTS

References:

"Beiträge zum Gesetze der Proportionalität von Tragheit und Gravität", R. von Eötvös, D Pekár, E. Fekete, *Annalen der Physik* **68**, 11, (1922)

"The Equivalence of Inertial and Passive Gravitational Mass" P.G. Roll, R. Krotkov, R.H. Dicke, *Annals of Physics* **26**, 442 (1964)

"Verification of the Equivalence of Inertial and Gravitational Mass" V.B. Braginsky, V.I. Panov, *Soviet Physics - JETP (English translation)* **34**, 463 (1972)
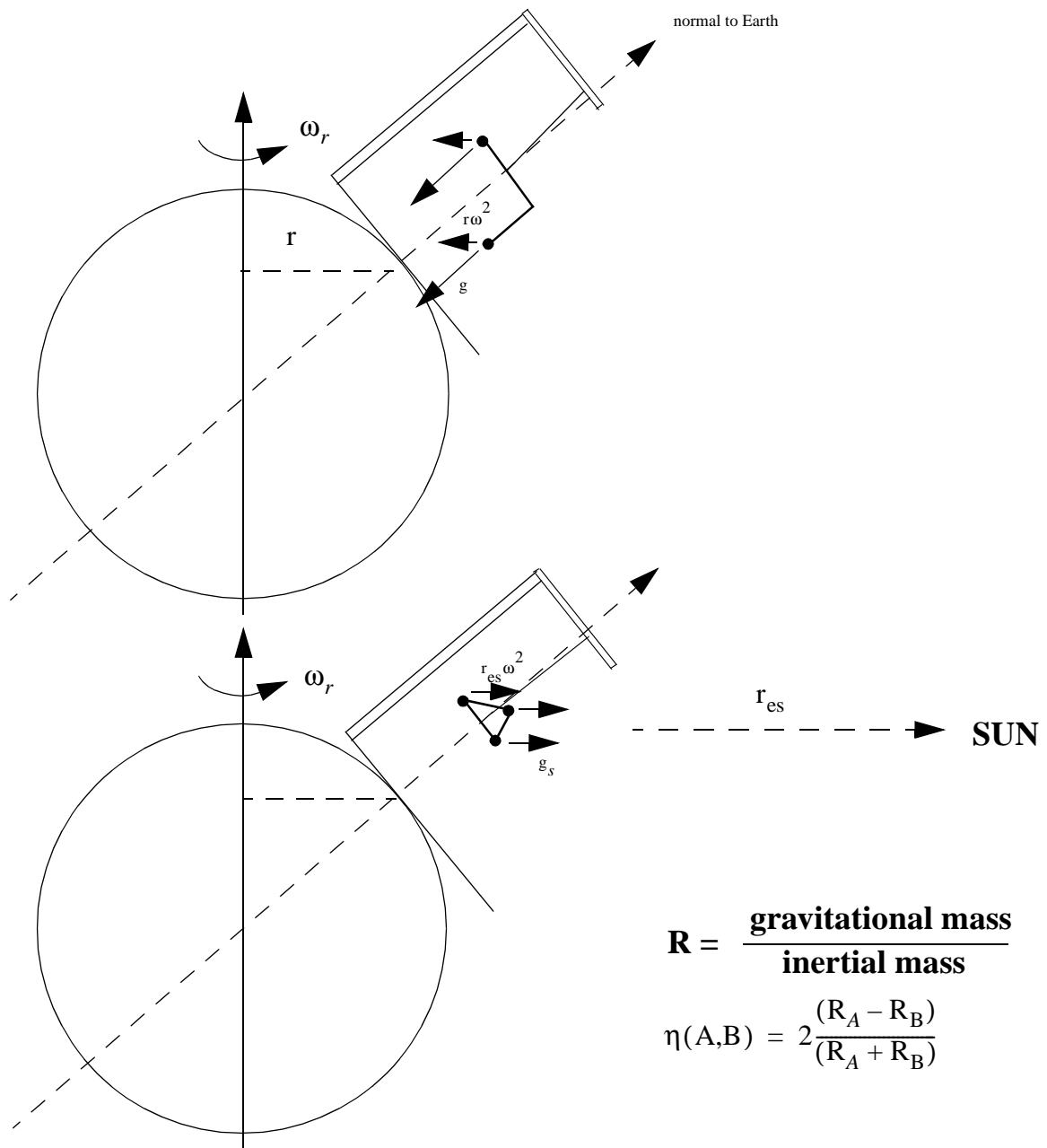
$$R = \frac{\text{gravitational mass}}{\text{inertial mass}}$$

$$\eta(A,B) = 2\frac{(R_A - R_B)}{(R_A + R_B)}$$

Labels on figure (top to bottom):
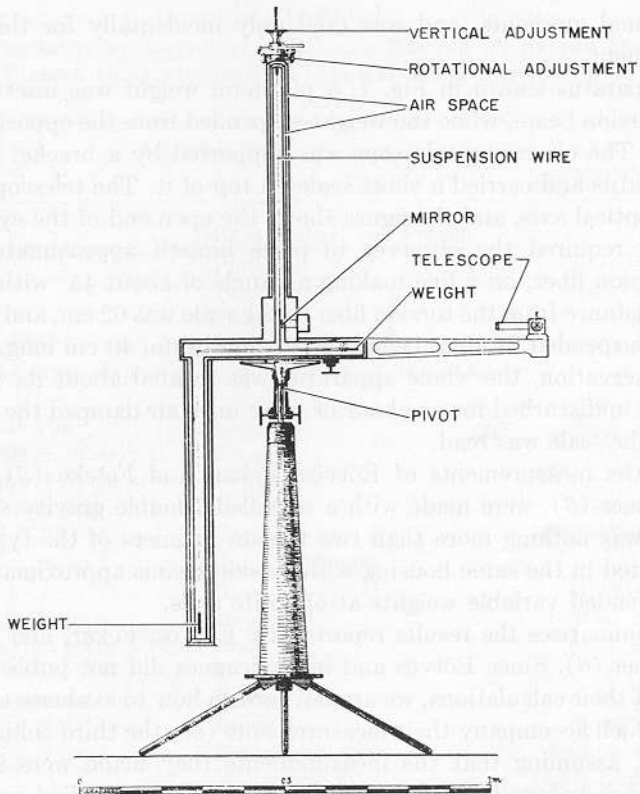- VERTICAL ADJUSTMENT
- ROTATIONAL ADJUSTMENT
- AIR SPACE
- SUSPENSION WIRE
- MIRROR
- TELESCOPE
- WEIGHT
- PIVOT
- WEIGHT

Materials		η (A,B) $\pm$ standard deviation of the mean
A	B	
Eötvös, Pekar, and Feteke		
Magnalium	Platinum	$(4 \pm 1) \times 10^{-9}$
Snakewood	Platinum	$(-1 \pm 2) \times 10^{-9}$
Copper	Platinum	$(4 \pm 2) \times 10^{-9}$
$Ag_2SO_4 + FeSO_4$ + glass and brass vials	Reacted Ag_2SO_4 + $FeSO_4$ + glass and brass vials	$(0 \pm 1) \times 10^{-9}$
Water + brass vial	Copper	$(-5 \pm 1) \times 10^{-9}$
$CuSO_4$ crystals + brass vial	Copper	$(-3 \pm 1) \times 10^{-9}$
$CuSO_4$ solution + brass vial	Copper	$(-4 \pm 1) \times 10^{-9}$
Asbestos + brass vial	Copper	$(-2 \pm 1) \times 10^{-9}$
Talc + brass	Copper	$(-3 \pm 1) \times 10^{-9}$
Renner[a]		
Platinum	Brass	$(0.45 \pm 0.65) \times 10^{-9}$
Batavian glass drops	Brass	$(-0.06 \pm 0.67) \times 10^{-9}$
Ground Batavian glass drops	Brass	$(0.21 \pm 0.65) \times 10^{-9}$
Paraffin + brass vial	Brass	$(0.24 \pm 0.26) \times 10^{-9}$
NH_4F + brass vial	Brass	$(0.06 \pm 0.25) \times 10^{-9}$
Copper	Manganese alloy	$(-0.08 \pm 0.20) \times 10^{-9}$
Copper	Manganese alloy	$(-0.12 \pm 0.22) \times 10^{-9}$
Bismuth	Brass	$(-0.14 \pm 0.74) \times 10^{-9}$

[a] As discussed in the text, the standard deviations given in this table for Renner's results should be increased by a factor of three.
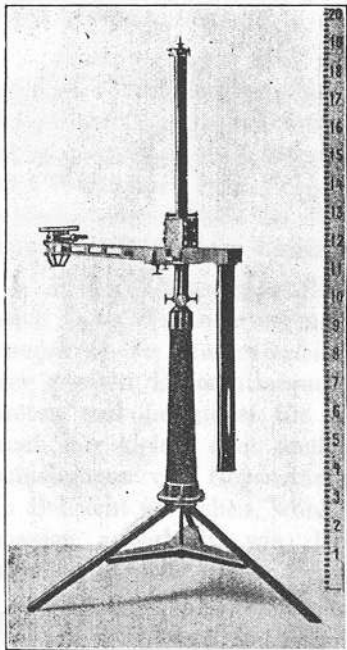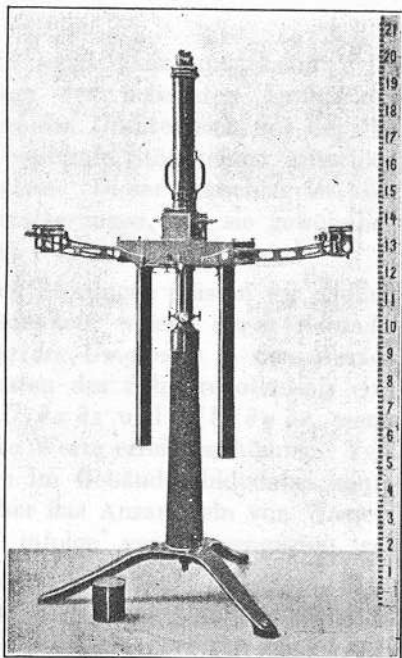
Fig. 6.　　　　　Fig. 7.

	$\varkappa - \varkappa_{\mathrm{Pt}}$
Magnalium	$+\,0{,}004 \cdot 10^{-6} \pm 0{,}001 \cdot 10^{-6}$
Schlangenholz	$-\,0{,}001 \cdot 10^{-6} \pm 0{,}002 \cdot 10^{-6}$
Kupfer	$+\,0{,}004 \cdot 10^{-6} \pm 0{,}002 \cdot 10^{-6}$
Wasser	$-\,0{,}006 \cdot 10^{-6} \pm 0{,}003 \cdot 10^{-6}$
Kristall. Kupfersulfat . . .	$-\,0{,}001 \cdot 10^{-6} \pm 0{,}003 \cdot 10^{-6}$
Kupfersulfatlösung	$-\,0{,}003 \cdot 10^{-6} \pm 0{,}003 \cdot 10^{-6}$
Asbest	$+\,0{,}001 \cdot 10^{-6} \pm 0{,}003 \cdot 10^{-6}$
Talg	$-\,0{,}002 \cdot 10^{-6} \pm 0{,}003 \cdot 10^{-6}$

Handwritten annotations:

NO (BRASS)

SINGLE BEMBER

DOUBLE BALANCE EXP

BRASS +
BRASS +
BRASS +
BRASS +
BRASS +

→ REFERENCE (next to Kupfer)

FROM P 34 (next to Magnalium)
FROM P 36 (next to Schlangenholz)
FROM P 37 (next to Kupfer)

CALCULATED BY TAKING XX DIFFERENCES WITH Cu VS Pt AND DATA ON PAIRS IN TEST
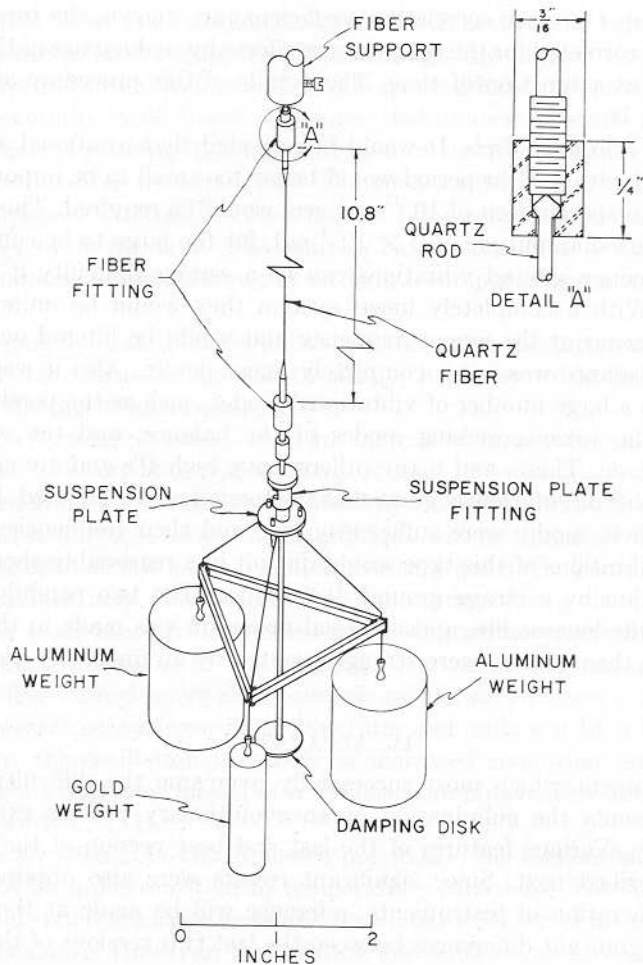
FIG. 3. The torsion balance suspension. The construction of both upper and lower fiber fittings is illustrated in Detail "A."
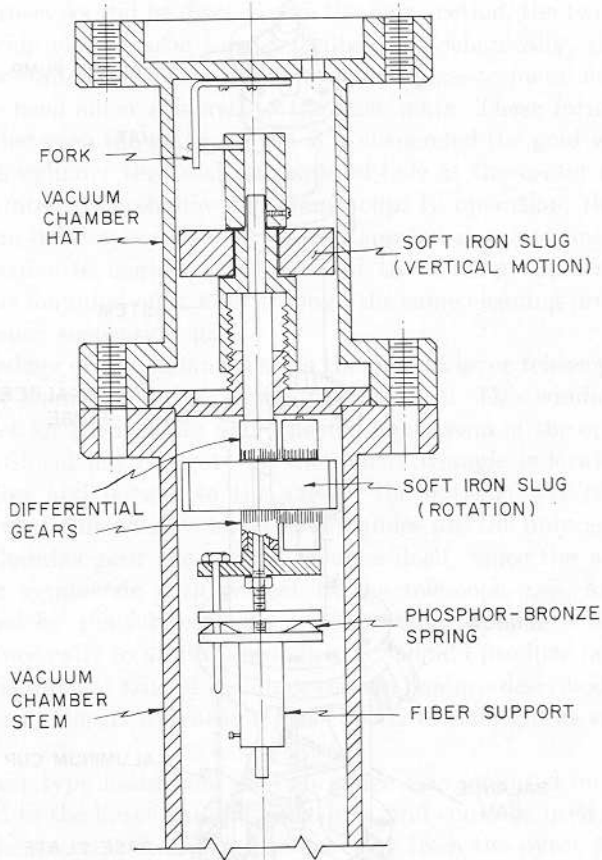
FIG. 4. Detail of the mechanism for independently raising and lowering, and rotating the torsion balance inside the vacuum chamber. Turning the lower soft iron slug with a magnet outside the vacuum chamber stem causes the torsion fiber to rotate slowly. The differential gears provide a 20:1 reduction ratio. Using a magnet outside the vacuum chamber hat to rotate the upper iron slug causes the torsion balance to move vertically over a span of about $\frac{1}{2}$ in. One revolution of the upper slug causes a vertical motion of $\frac{1}{20}$ in.
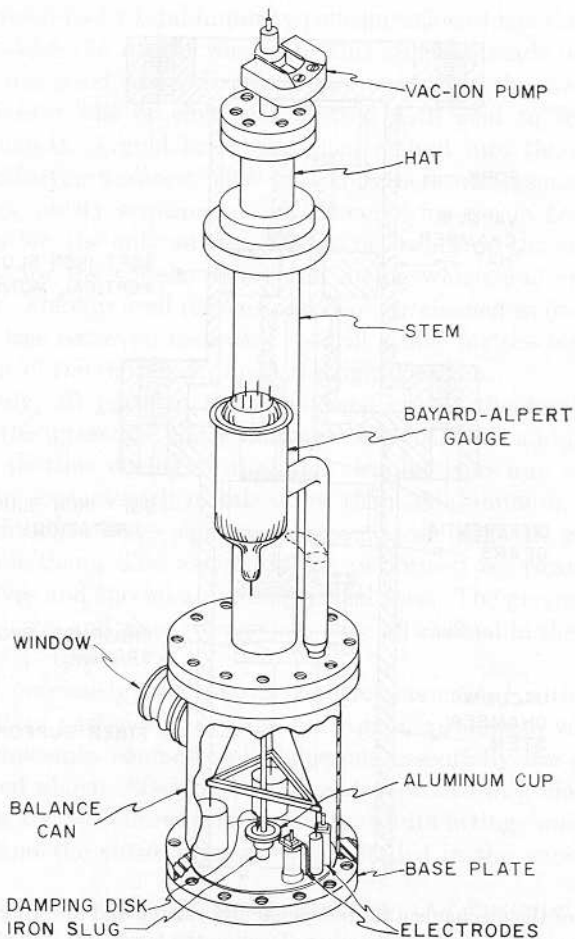
FIG. 5. Cutaway drawing of the vacuum chamber showing the torsion balance in place. Flanges are sealed with gold "O" rings.
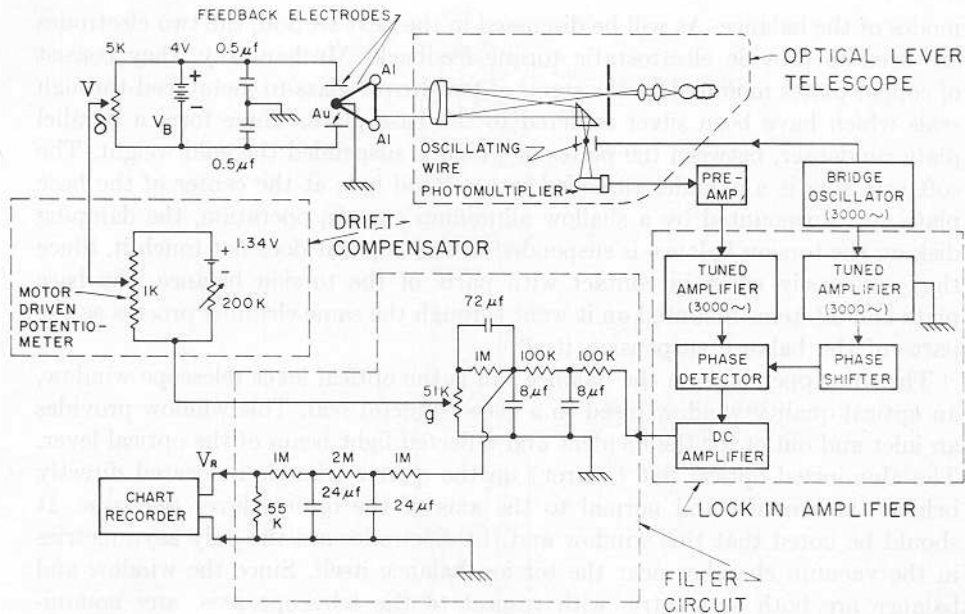
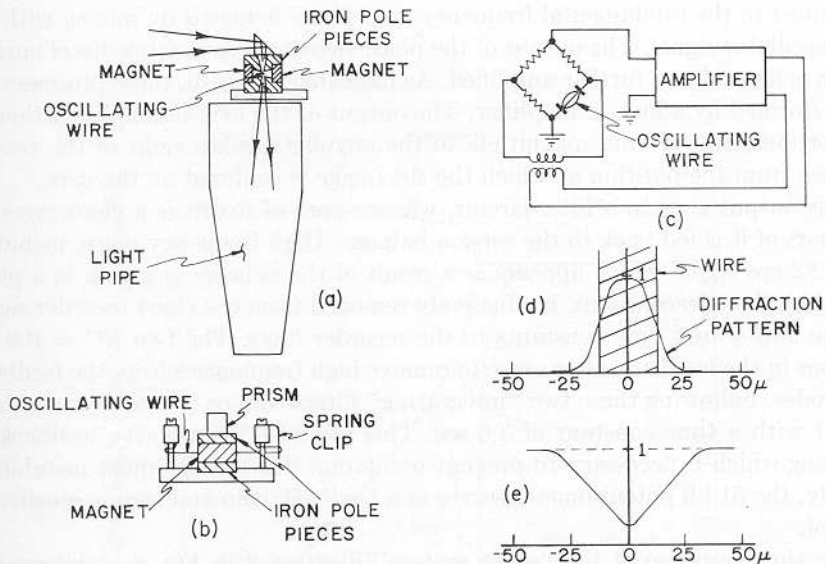Fig. 6. Block diagram of the optical lever detection system

FIG. 7. Details of the oscillating wire light modulator. (a) Top view of the oscillating wire device, showing the magnet and pole piece assembly, prism, and light pipe. (b) Side view, showing the method of mounting the oscillating wire between the pole pieces. (c) Block diagram of the balanced bridge oscillator which drives the oscillating wire. (d) Sketch of the diffraction image of the slit focused and centered on the equilibrium position of the oscillating wire. As the wire oscillates about the position illustrated, the light received by the photomultiplier is modulated at the second harmonic of the wire frequency. Only when the diffraction image shifts off-center from the equilibrium position of the wire is the fundamental wire frequency detected by the photomultiplier. (e) Calculated fractional light intensity received by the photomultiplier as a function of displacement of the diffraction image of the slit from the center of the wire.

Difficulties in Eötvös's experiment:
     Apparatus not designed for the job - it was a gravity gradiometer in an earlier life

     Gravity gradients - Eötvös himself a significant perturbation

     Magnetic field sensitivity - material problems in all manufactured substances.

     Thermal gradients - radiometer effect - the wrong way instrument in the jewelers window

     Temperature variations - change in torsion offset and torsion constant

     Fluctuations in the surface charge on the housing and the masses - patch effect variations

     Seismic noise

     Brownian motion of the low Q system in air

Procedures attempted to improve the experiment:
     Solar g and rotation of apparatus by earth - first idea, 1/f noise too large (a (earth/sun) = 4 @ latitude of 45 deg)

     Beat 1/f noise by modulation - turning the suspension - gravity gradients and insufficient damping

     Attempt to make differential - two suspensions in the same envelope - too much common mode noise

Critical improvements made in the Dicke version:
     Operation in ultra high vacuum -
          elimination of noisy damping
          elimination of radiometer effect
          stabilization of patch effect (though not completely removed)

     Significant reduction of sensitivity to gravitational gradients due to mass configuration

     Fused silica suspensions and multiple-refined materials to reduce magnetic impurities

     Closed loop servo system to damp the system and measure the rotation

     Angle sensor operating at the fundamental noise limit due to suppressed carrier modulation to provide the (almost noise free) feedback signal.

     Reduction in 1/f noise from improvements to allow solar modulation
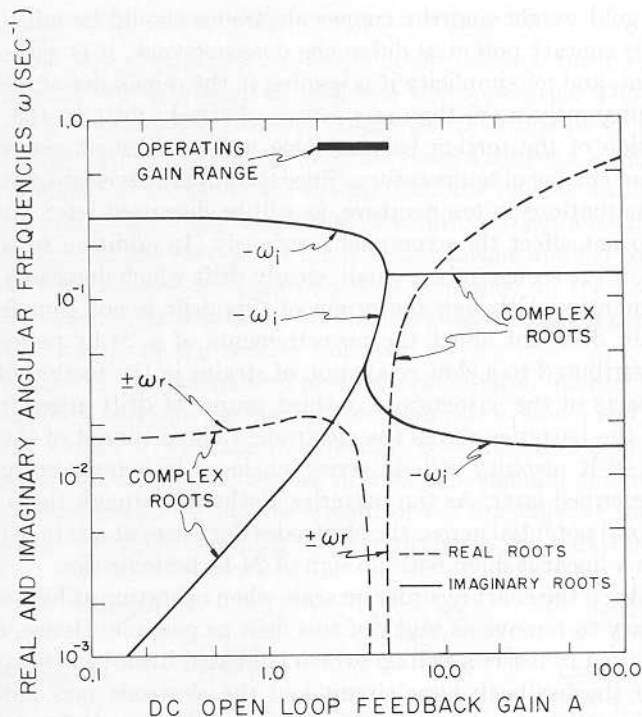
     Operation in a thermally controlled environment

Fig. 8. Resonant angular frequencies of the torsion balance system as a function of the dc open loop feedback gain A. The dashed curves represent real parts of the resonance frequencies, while the solid curves represent imaginary parts which lead to damping of torsional oscillations. Also shown as solid curves are purely imaginary roots. The curves were calculated from the transfer characteristic of the feedback filter circuit shown in Fig. 6.
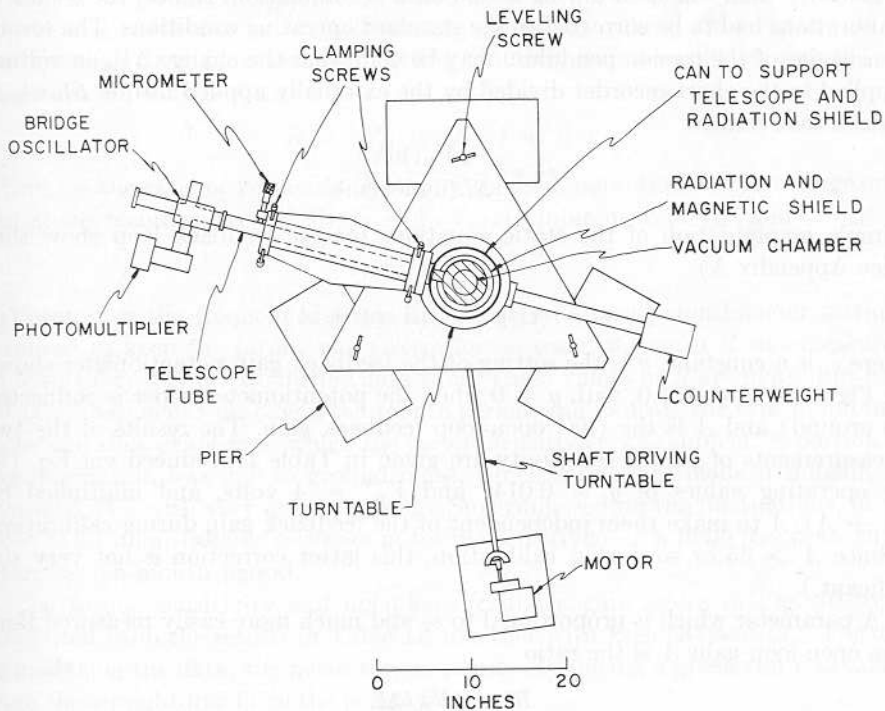
FIG. 9. Schematic top view of the torsion balance mounted in the instrument well
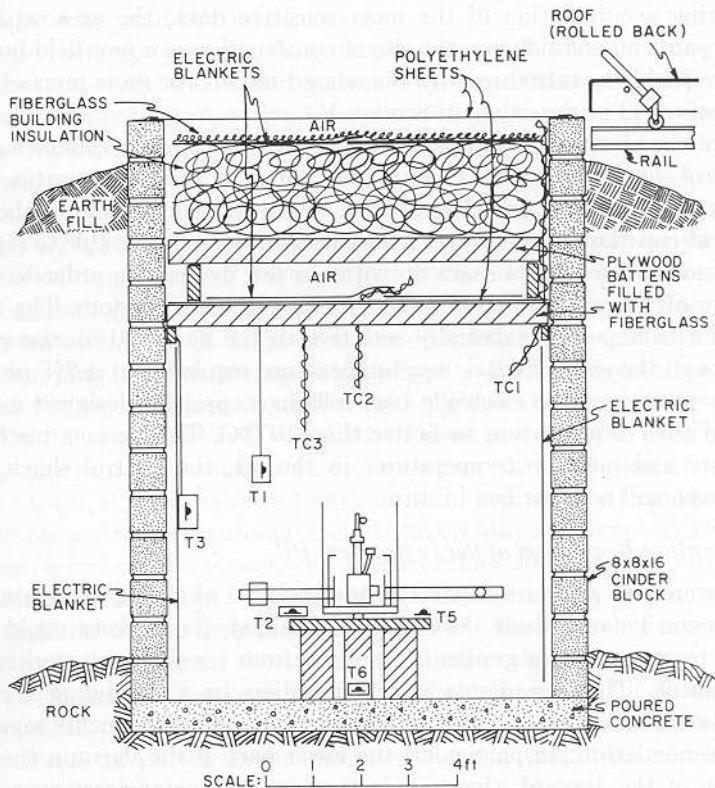
INSTRUMENT PIT

FIG. 11. Schematic cutaway drawing of the instrument well with the torsion balance installed. TC1, TC2, and TC3 are thermocouples used to measure temperature gradients between various points in the well and the insulation plug. T1, T2, T3, T5, and T6 are thermistor temperature sensors which were used in Wheatstone bridge circuits to monitor very small (10^{-3}°C) temperature changes near the torsion balance.

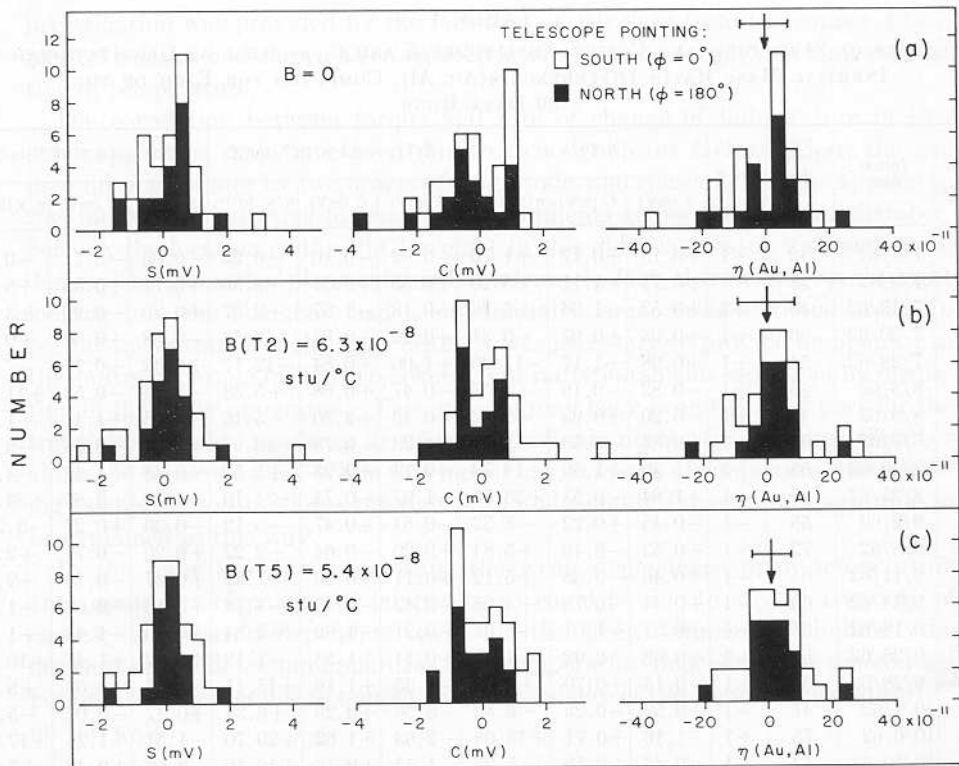FIG. 19. Distributions of amplitudes of sine and cosine coefficients S and C in the least squares fit of $(S \sin t + C \cos t + K)$ to the torsion balance torque output. t is the local solar time in radians (local solar noon = $0, 2\pi, \cdots$). The third column shows histograms of values of $\eta(\text{Au, Al}) = (S/\cos D \cos \varphi)$ for the 39 data runs, with the arrows and horizontal cross bars indicating mean values and widths (standard deviations) of the distributions, respectively. Orientation of the optical lever telescope is indicated by the shading of the bars in the histograms. (a) Distributions obtained without subtraction of a temperature regression from the torque. (b) Distributions obtained after subtracting a regression with thermistor no. 2 (T2) from the torque. (c) Distributions obtained after subtracting a regression with thermistor no. 5 (T5) from the torque. Numerical values displayed on the above histograms are given in Table V.

TABLE VI

Mean Values of η(Au, Al), with Probable Errors of the Mean[a]

Points more than 3 std. dev. from mean excluded	Telescope orientation	No temperature regression subtracted ($B(T2) = 0$)	T2 regression subtracted ($B(T2) = 6.3 \times 10^{-8}$ stu/°C)	T5 regression subtracted ($B(T5) = 5.4 \times 10^{-8}$ stu/°C)
No	North	$(+2.22 \pm 1.42) \times 10^{-11}$	$(1.38 \pm 1.27) \times 10^{-11}$	$(1.30 \pm 1.25) \times 10^{-11}$
No	South	$(-2.53 \pm 1.94) \times 10^{-11}$	$(-0.25 \pm 2.70) \times 10^{-11}$	$(1.33 \pm 1.73) \times 10^{-11}$
No	North + South	$(-0.09 \pm 1.20) \times 10^{-11}$	$(0.59 \pm 1.45) \times 10^{-11}$	$(1.32 \pm 1.04) \times 10^{-11}$
Yes	North	$(+2.22 \pm 1.42) \times 10^{-11}$	$(1.38 \pm 1.27) \times 10^{-11}$	No values more than 3 std. dev. from mean
Yes	South	$(-0.59 \pm 1.51) \times 10^{-11}$	$(2.44 \pm 2.00) \times 10^{-11}$	
Yes	North + South	$(+0.89 \pm 1.03) \times 10^{-11}$	$(1.94 \pm 1.15) \times 10^{-11}$	

[a] The means and their probable errors for the 20 runs with the optical lever telescope oriented north and the 19 runs with it oriented south are presented separately in rows 1, 2, 4, and 5, while rows 3 and 6 contain the corresponding results for all 39 runs averaged together. Results are given with no temperature effects removed (column 3), after subtracting the regression with thermistor no. 2 output (column 4), or after subtracting the regression with thermistor no. 5 output (column 5). The two runs with values of η more than three standard deviations from the mean have been excluded in rows 4, 5, and 6, but are included in the first three rows.

Limitations of the Dicke experiment:

Non-Gaussian nature of the seismic noise at 24 hour periods, in part due to rectification of high frequency seismic noise by non-linearities in the suspension.

A residual thermal coupling to the suspension (never completely understood).

Results of the Dicke experiment

- $\eta(\text{Al,Au}) \leq 10^{-11}$ later surpassed by Braginsky to a limit of 10^{-12} and now by another factor of 10 by Adelberger.
- **The experiment showed all of us how to control a mechanical system and how to approach the fundamental limits of the experiment design.**

Kip's flirtations with being an experimenter

The relevant attribute of an experimenter: Putting your tochis[1] on the line and living with your decision.

- **The LIGO beamtube scattering and the baffle design.**

    "*Scattered-Light Noise for LIGO* " E. E. Flanagan and K.S. Thorne, LIGO Technical Report T950132-00-R (1995); the final article of many years of thinking about the problem.

A significant contribution to the design and construction of LIGO

    showed the way to make the calculation
    determined the baffle spacing
    established the proper formulation for the baffle serrations

- **Gravity-gradient noise in LIGO**

" Seismic gravity-gradient noise in interferometric gravitational-wave detectors" S. Hughes, K.S. Thorne, *Physical Review D* **58**, 122002-1, (1998).

Propose making moats in the ground to stop the propagation of Rayleigh waves which produce density fluctuations in the ground around the test masses. Moats might be 35 meters in diameter and 10 meters deep (the authors do recognize the special problems with the moats in Louisiana.)

"Human Gravity-Gradient Noise in Interferometric Gravitational-Wave Detectors" K.S.Thorne, C.J. Winstein, Physical Review D **60**,082001, (1999)

The way we walk causes time dependent gravitational gradients. Think twice about letting people next to the machine when observing.

---

1. "ass" defined in " *The Joys of Yiddish*" Leo Rosten, Mc Graw Hill (1968)